

# Towards the full quantum dynamical description of photon induced processes in $D_2^+$

A. Tóth,<sup>1</sup> S. Borbély,<sup>2,\*</sup> G. Zs. Kiss,<sup>2</sup> G. J. Halász,<sup>3</sup> and Á. Vibók<sup>1,4,†</sup>

<sup>1</sup>*Department of Theoretical Physics, University of Debrecen,*

*H-4010 Debrecen, PO Box 5, Hungary*

<sup>2</sup>*Faculty of Physics, Babeş-Bolyai University,*

*Kogălniceanu Street 1,400084 Cluj Napoca, Romania*

<sup>3</sup>*Department of Information Technology, University of Debrecen,*

*H-4010 Debrecen, PO Box 12, Hungary*

<sup>4</sup>*ELI-ALPS, ELI-HU Non-Profit Ltd,*

*H-6720 Szeged, Dugonics tér 13, Hungary*

(Dated: July 12, 2021)

## Abstract

A new quantum dynamical model has been developed to describe the dissociative ionization of deuterium molecular ions by intense laser pulses ( $\tau = 10$  fs,  $\lambda = 200$  nm and  $I = 3 \times 10^{13}$  W/cm<sup>2</sup>). We calculated the ionization probability densities by solving the time-dependent Schrödinger equation numerically. Throughout the simulation the nuclear vibration was considered as a dynamic variable with fixed molecular axis orientation. Benchmark calculations were performed for the ionization of HeH<sup>++</sup>, for which accurate numerical results are available in the literature, in order to check the performance of this new restricted model.

---

\* sandor.borbely@phys.ubbcluj.ro

† vibok@phys.unideb.hu

## I. INTRODUCTION

The dynamics initiated in a molecule by photon impact is usually discussed in terms of the Born-Oppenheimer (BO) approximation [1], where fast moving electrons are treated separately from the slow nuclei. In this scheme, electrons and nuclei do not easily exchange energy. However, this energy exchange can become important in some nuclear regions, particularly in the vicinity of degeneracy points or conical intersections (CIs) [2–7]. It is widely recognized today that conical intersections are very important in the nonadiabatic processes which are ubiquitous in photophysics and photochemistry.

For diatomic molecules, which have only one degree of freedom, it is not possible for two electronic states of the same symmetry to become degenerate and, as a consequence of the well-known noncrossing rule, an avoided crossing results. However, this is only true in free space. It has been shown in previous papers that conical intersections can be created even in diatomics [8, 9] both by running or by standing laser waves. In this situation the laser-light couples either the center of mass motion with the internal rovibrational degrees of freedom (in case of a standing laser field) or the vibrational motion with the emerged rotational degree of freedom (in case of a running laser field) resulting in a so-called light-induced conical intersection (LICI). The position of the LICI is determined by the laser frequency, while the laser intensity controls the strength of its nonadiabatic coupling.

A few years ago, we have started a systematic study of the nonadiabatic effect induced by laser fields in molecular systems and demonstrated that the light-induced conical intersections have a significant impact on several dynamical properties (like the molecular spectra, the molecular alignment etc.) of diatomic molecules [10–17].

The photodissociation and ionization processes of the  $D_2^+$  ion have been thoroughly studied for more than quarter of a century [18–65]. In our recent papers, we have also investigated the dissociation dynamics of the  $D_2^+$  in the LICI picture starting the initial nuclear wave packet either from different vibrational eigenstates or from the Franck–Condon distribution of the vibrational states obtained from photoionizing  $D_2$  [14–17]. One (1D) and two-dimensional (2D) calculations have been performed and compared to each other. In the 1D model, the molecular rotational angle was only a parameter, i. e. the LICI was not considered, whilst in the 2D scheme the rotational angle was assumed as a dynamic variable thereby explicitly incorporating the LICI. The obtained 1D and 2D results strongly

differ, demonstrating the significant impact of the LICI on the  $D_2^+$  dissociation dynamics. Additionally, in a recent letter [17], we were able to provide the first “direct observable and measurable signature” of the light-induced conical intersections by studying carefully the dissociation process of  $D_2^+$ .

This article is our initial attempt to combine the photodissociation and ionization of  $D_2^+$  using a newly developed restricted model which assumes fixed molecular axis orientations. Beside the previously considered [14–17] ground and first excited states, this model includes an ionized state with a well defined asymptotic electron momentum  $\vec{k}$ . For this three-level system, the time-dependent nuclear Schrödinger equation was solved numerically and the ionization probability density for the fixed  $\vec{k}$  electron momentum was extracted from the final population of the ionized state. The ionization probability density for the whole electron continuum was mapped by performing several independent calculations for the different electron momentum values.

Using the above outlined approach, we have investigated the ionization spectrum of  $D_2^+$  for previously studied conditions [14–17], where the formation of the LICI between the ground and the first excited state has been observed. Our model has also been used to investigate the ionization of  $HeH^{++}$  at fixed molecular axis lengths, for which accurate numerical results are available in the literature [51, 52].

This article is divided in four sections. The introduction is followed by the presentation of the required methods and algorithms as well as the calculated dynamical quantities. The third section presents and discusses the  $D_2^+$  and the  $HeH^{++}$  numerical results. In the last section the conclusions and future plans are summarized.

## II. THEORY AND METHODS

Our theoretical approach for laser driven ionization and dissociation dynamics is an extension of a previous model that described the dissociation of  $D_2^+$  molecular ion [14–17]. The original model describes nuclear dynamics only for the two relevant electronic energy levels corresponding to the ground and the first excited states. The extended model includes a third energy level corresponding to an electronic continuum state defined by its asymptotic electron momentum  $\vec{k}$ . The wave packets contributing to the nuclear wave function for this

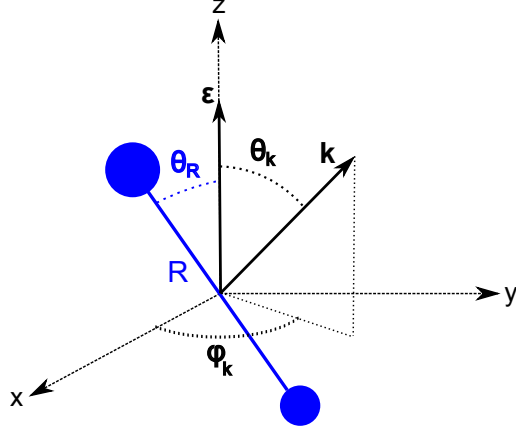


FIG. 1: The geometry of the studied system in a reference frame defined by the laser polarization ( $\varepsilon \in Oz$ ) and by the molecular axis ( $R \in xOz$ ). The ejected electron is described by the  $\vec{k}$  asymptotic momentum vector.

model system can be arranged in a vector form as follows

$$\Psi_N(R; \theta_R) = \begin{pmatrix} \Psi_G(R; \theta_R) \\ \Psi_X(R; \theta_R) \\ \Psi_I(R; \theta_R) \end{pmatrix}, \quad (1)$$

where  $\Psi_G(R; \theta_R)$  is the vibrational wave packet on the ground state,  $\Psi_X(R; \theta_R)$  is the wave packet on the excited state, while  $\Psi_I(R; \theta_R)$  is the wave packet on the ionization level.  $R$  denotes the internuclear separation between the nuclei, while  $\theta_R$  is the angle between the internuclear axis and the polarization axis of the external laser pulse. The geometrical arrangement of the studied system is shown in Figure 1. In the current calculations,  $\theta_R$  is considered only as a parameter and the nuclear wave packet dynamics is solved explicitly only for the vibrational degree of freedom. The field free Hamiltonian of the system can be written as

$$H_0 = \begin{pmatrix} -\frac{1}{2\mu} \frac{\partial^2}{\partial R^2} + V_G(R) & 0 & 0 \\ 0 & -\frac{1}{2\mu} \frac{\partial^2}{\partial R^2} + V_X(R) & 0 \\ 0 & 0 & -\frac{1}{2\mu} \frac{\partial^2}{\partial R^2} + V_I(R) \end{pmatrix}, \quad (2)$$

where  $\mu = M_1 M_2 / (M_1 + M_2)$  is the reduced mass of the system and  $V_{\{G,X,I\}}(R)$  are the potential energy surfaces of the ground ( $G$ ), the first excited ( $X$ ) electronic, as well as the

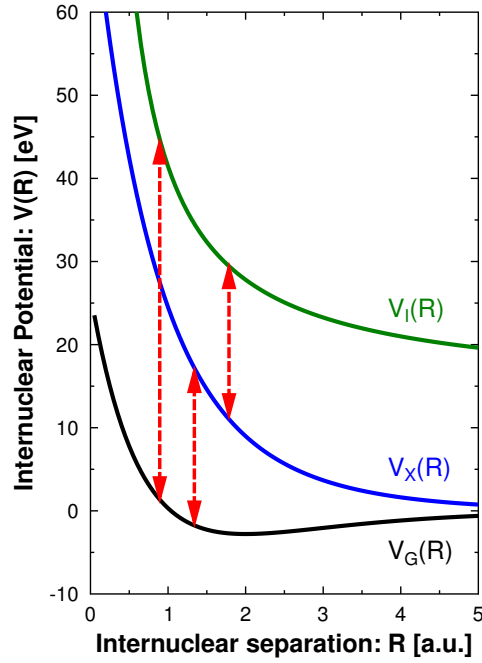


FIG. 2: A schematic picture of the potential energy surfaces considered in the present model showing three energy levels: the ground  $V_G(R) = 1s\sigma_g$ , the first excited  $V_X(R) = 2\pi\sigma_u$  and the ionization level  $V_I(R)$  (with  $k = 0.2$  a.u.) of  $D_2^+$ . The radiative couplings between the different energy levels are indicated by dashed arrows.

ionic ( $I$ ) states of the  $D_2^+$  ion. These potential energy surfaces can be expressed as a sum of the electronic energy and Coulomb repulsion between the atomic nuclei:

$$V_{\{G,X,I\}}(R) = E_{\{G,X,I\}}(R) + \frac{Z_1 Z_2}{R}, \quad (3)$$

with  $Z_1$  and  $Z_2$  being the charge of the nuclei.

Figure 2 shows that the origin of the potential energy axis is fixed to the asymptotic value of the ground state potential energy surface. Coupling between the different levels is possible in the presence of an external laser pulse and is described by the interaction term

of the Hamiltonian:

$$H_{int} = \begin{pmatrix} 0 & -\vec{\varepsilon} \cdot \vec{d}_{GX} F(t) & -\vec{\varepsilon} \cdot \vec{d}_{GI} F(t) \\ -\vec{\varepsilon} \cdot \vec{d}_{XG} F(t) & 0 & -\vec{\varepsilon} \cdot \vec{d}_{XI} F(t) \\ -\vec{\varepsilon} \cdot \vec{d}_{IG} F(t) & -\vec{\varepsilon} \cdot \vec{d}_{IX} F(t) & 0 \end{pmatrix}, \quad (4)$$

where  $\vec{d}_{ij}(R, \theta_R) = \langle \psi_i^e(\vec{R}, \vec{r}) | \vec{r} | \psi_j^e(\vec{R}, \vec{r}) \rangle$  are the transition dipole moments between the electronic states described by the  $\psi_i^e$  and  $\psi_j^e$  wave functions and  $F(t)$  is the electric component of the employed laser pulse. Sine-square shaped laser pulses are used throughout the calculations:

$$F(t) = \begin{cases} F_0 \cos(\omega t) \sin^2(\frac{\pi t}{\tau}) & \text{if } t \in (0, \tau) \\ 0 & \text{elsewhere} \end{cases}, \quad (5)$$

where  $\omega$  is the carrier wave frequency,  $F_0$  is the amplitude of the electric field and  $\tau$  is the duration of the laser pulse. The time evolution of the nuclear wave function (1) is governed by the time-dependent Schrödinger equation:

$$i \frac{\partial \Psi_N(R, t; \theta_R)}{\partial t} = (H_0 + H_{int}) \Psi_N(R, t; \theta_R). \quad (6)$$

In the present approach, this Schrödinger equation (6) is solved using the efficient multi-configurational time-dependent Hartree (MCTDH) package [66–71]. To describe the vibrational degree of freedom the Fast Fourier Transformation-Discrete Variable Representation (FFT-DVR) was used, with  $N_R$  basis elements distributed on the range from 0.1 a.u. to  $R_{\max}$ . The vibrational wave function can be expressed as a function of this FFT-DVR basis set ( $\chi_j(R)$ ) as:

$$\Psi(R, t) = \sum_{j=1}^{N_R} c_j(t) \chi_j(R). \quad (7)$$

A complex absorbing potential (CAP) is applied to all three energy levels considered in our model. It has the following form

$$-iW(R) = \begin{cases} 0 & \text{if } R < R_0 \\ -i\eta(R - R_0)^3 & \text{if } R \in [R_0, R_{\max}] \end{cases}, \quad (8)$$

where  $\eta$  is the strength, and  $R_0$  is the starting point of the CAP. In our model, the CAP prevents the reflection of the wave function's dissociative part at the simulation box boundary and helps to monitor the absorbed wave function norms at each energy level, which are subsequently used to calculate physical observables. After initialization, the nuclear wave packet (1) is propagated numerically in time according to the Schrödinger equation (6) using the 6th order Adams-Bashforth-Moulton (ABM) predictor-corrector method with variable time-steps. The value of the numerical parameters used during the numerical solution of the Schrödinger equation (6) are presented along the results obtained for each investigated system.

### A. The electronic Schrödinger equation

Beside the accurate solution of the nuclear time-dependent Schrödinger equation (6) the most important part of the proposed work is the accurate calculation of the electronic energy levels  $E_{\{G,X,I\}}(R)$  and of the transition dipole moments between them. In order to achieve this goal, the one-electron stationary Schrödinger equation for diatomic molecules is solved with the electronic Hamiltonian written as:

$$H^e = \frac{\hat{p}_e^2}{2} - \frac{Z_1}{r_1} - \frac{Z_2}{r_2}, \quad (9)$$

where  $r_1$  and  $r_2$  are the electron coordinates measured from the nuclei. From practical purposes it is more convenient to convert the electronic Hamiltonian (9) into prolate spheroidal coordinates:

$$H^e = -\frac{2}{R^2(\xi^2 - \eta^2)} \left[ \frac{\partial}{\partial \xi} (\xi^2 - 1) + \frac{\partial}{\partial \xi} \frac{\partial}{\partial \eta} (1 - \eta^2) \frac{\partial}{\partial \eta} + \frac{1}{\xi^2 - 1} \frac{\partial^2}{\partial \phi^2} + \frac{1}{1 - \eta^2} \frac{\partial^2}{\partial \phi^2} \right] - \frac{2}{R} \left[ \frac{\xi(Z_1 + Z_2) + \eta(Z_1 - Z_2)}{\xi^2 - \eta^2} \right], \quad (10)$$

where  $R$  is the fixed internuclear distance, while the  $\eta$  and  $\xi$  coordinates are obtained using the following transformations:

$$\xi = \frac{r_1 + r_2}{R}, \quad (11)$$

$$\eta = \frac{r_1 - r_2}{R}. \quad (12)$$

In the next step, the above Hamiltonian (10) was discretized using a finite-element discrete variable representation (FEDVR) numerical grid [72] for the  $\eta$  and  $\xi$  coordinates. The  $\phi$  coordinate can be discretized on the  $e^{im\phi}$  trigonometric basis. In the present case we were looking for cylindrically symmetric solutions, meaning that this basis could be reduced to  $m = 0$ , therefore in (10) the  $\phi$  dependent terms were omitted altogether. The eigenvalues and eigenvectors of the obtained Hamiltonian matrix were calculated using the SLEPc [73] eigensolver package. Further technical details on the above outlined procedure can be found in [74].

After performing detailed convergence checks, the accurate electronic wave functions ( $\Psi_{\{G,X\}}^e(R)$ ) and electronic energies ( $E_{\{G,X\}}^e(R)$ ) for the ground and excited states were obtained at all internuclear distances considered during the nuclear wave packet dynamics. The electronic energy for the ionization level is given by:

$$E_I(R) = \frac{k^2}{2}. \quad (13)$$

For the description of the ionization states, simple one-center momentum normalized Coulomb wave functions [75] have been used:

$$\psi_c(\vec{k}, \vec{r}) = \sqrt{\frac{2}{\pi}} \frac{1}{kr} \sum_{lm} i^l e^{i\sigma_l} Y_{lm}^*(\hat{k}) Y_{lm}(\hat{r}) F_l(\gamma, kr), \quad (14)$$

where  $F_l$  are the radial Coulomb functions,  $\gamma = -(Z_1 + Z_2)/k$  is the Sommerfeld parameter, and  $\sigma_l = \arg(\Gamma(l + 1 + i\gamma))$  is the Coulomb phase shift. As the Coulomb wave functions are "state density" functions, they need to be discretized by dividing the momentum space into small boxes with a  $\delta V$  volume centered around the  $\vec{k}$  momentum vector. As a result of this discretization all continuum states in this  $\delta V$  volume element can be collectively described

by the  $\psi_I^e(\vec{k}, \vec{r})$  wave function, which can be written as

$$\psi_I^e(\vec{k}, \vec{r}) = \sqrt{\delta V} \psi_c(\vec{k}, \vec{r}). \quad (15)$$

The calculation of the potential energy surfaces and of the transition dipole moments is straightforward from these wave functions and their corresponding eigenenergies.

### B. Calculation of observables

After the end of the laser pulse (5), the system is propagated further in time until on each energy level, the dissociative part of the nuclear wave packets reached the end of the simulation box, where they are absorbed by the CAPs. The norm of these absorbed wave packets gives the probability of dissociation from each level. The ionization level is a special case as the norm of the nuclear wave packet at the end of the laser pulse also gives the probability of ionization into the  $\delta V$  momentum volume element:

$$P(\delta V, \vec{k}) = |\langle \Psi_I(R, t > \tau) | \Psi_I(R, t > \tau) \rangle|^2. \quad (16)$$

For all molecular systems studied here, the ionization level is purely dissociative, thus the searched  $P(\delta V, \vec{k})$  probability is equal with the wave function norm absorbed by the CAP placed on the ionization level. By dividing the probability (16) with the  $\delta V$  volume element the ionization probability density is obtained:

$$P(\vec{k}) = \lim_{\delta V \rightarrow 0} \frac{P(\delta V, \vec{k})}{\delta V}. \quad (17)$$

In order to map this ionization probability density independent calculations for all relevant  $\vec{k}$  values must be performed.

### C. Limitations of the model

The main limitation of the above outlined model is rooted in its design: the ionization probability densities for each ionization channel are calculated separately. This implies that the direct and indirect (through the ground and excited states) population transfer

between the ionization channels is not permitted. This shortcoming of our model may have an important impact on the calculated ionization probability densities at high laser field intensities where the continuum-continuum transitions and the depletion of the ground state play an important role in the ionization dynamics. As the model is designed to be used in situations where the dissociation and ionization have a comparable importance, we believe that this limitation will not have a significant impact on the obtained results.

### III. RESULTS AND DISCUSSION

The previously presented model has been used to study the ionization of  $D_2^+$  molecular ion by ultrashort laser pulses. The laser pulse parameters were those from our previous calculations [14–17], where LICI formation between the ground and the first excited state has been observed and multiphoton ionization is the dominant ionization mechanism.

The ionization of the  $HeH^{++}$  molecule at fixed molecular axis lengths in the single-photon ionization regime has been investigated to benchmark the new model. This system has been chosen as there are high precision differential results available [51, 52], and the *ab initio* results can be directly compared to simple first order perturbation calculations.

#### A. The $D_2^+$ ion

In this subsection, we show detailed analysis of the photoelectron distributions obtained by further ionizing a  $D_2^+$  molecular ion. The initial nuclear wave packet was obtained by transferring the vibrational ground state of the neutral molecule to the ground electronic state of the ion. The dynamics of this Franck–Condon wave packet was driven by a 10 fs long laser pulse with a 200 nm wavelength of the carrier wave and  $3 \times 10^{13}$  W/cm<sup>2</sup> intensity. We only considered fixed molecular axis orientations as this is the first step in working toward our long-term goal of the complete dynamical description of diatomic molecules.

##### 1. Numerical details

A simulation box with  $R_{max}=30$  a.u. size and  $N_R=768$  gridpoints was used for the present calculations. A CAP with  $R_0=20$  a.u. and  $\eta = 0.00005$  was applied to the ground state,

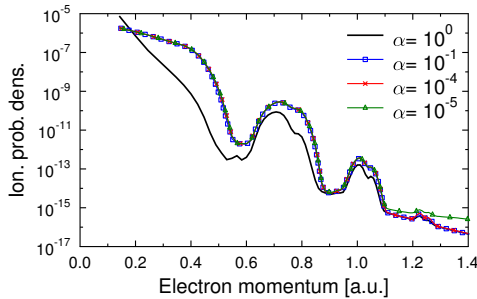


FIG. 3: Ionization probability density of the  $D_2^+$  along the internuclear axis for different values of the  $\alpha$  parameter. The molecular axis is parallel to the laser polarization  $\hat{\epsilon}$ . The parameters of the driving laser field:  $\lambda = 200$  nm,  $I_0 = 3 \times 10^{13}$  W/cm $^2$ ,  $\tau = 10$  fs.

while a CAP with  $R_0 = 25$  a.u. and  $\eta = 0.00236$  was used on the excited and ionization states. These parameters allow an accurate representation of the nuclear wave packets on the considered electronic states, and prevent the absorption of the nuclear wave packets during the action of the laser pulse.

The electronic states and the transition dipole moments between them were calculated by solving the electronic Schrödinger equation directly, as outlined in subsection II A. The numerical convergence of the calculated  $\Psi_G(R)$  and  $\Psi_X(R)$  was carefully verified and the derived potential energy surfaces and the dipole transition moments were compared to data found in the literature [76, 77] and a good agreement was found.

The correct selection of the  $\delta V$  volume element used during the discretization of the momentum space, and during the calculation of the ionization probability densities (17) is an important component of the present approach. In this model, we have fixed this volume element to be

$$\delta V = \alpha k^2, \quad (18)$$

where  $k$  is the magnitude of the electron momentum. The optimal value of the  $\alpha$  parameter was obtained from the convergence tests performed for the laser pulse parameters used in the calculations. The results of this convergence test are shown on Figure (3), where the ionization probability density for electrons ejected along the molecular axis are shown for different values of the  $\alpha$  parameter.

During the convergence tests, it was observed that a large  $\alpha$  value leads to erroneous results for the low energy electrons (see the  $\alpha = 1$  line) while a diminutive  $\alpha$  value (see the  $\alpha = 10^{-5}$  line) leads erroneous results for high energy electrons. Despite this, a large interval

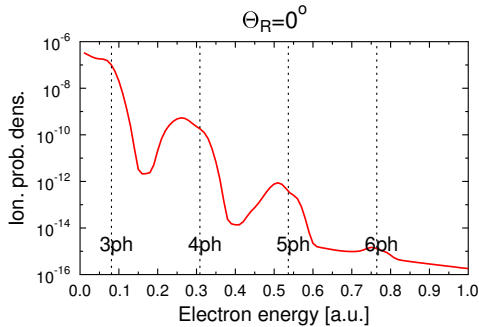


FIG. 4: Angle integrated ionization probability density as a function of electron ejection energy for the  $\theta_R = 0^\circ$  molecular axis orientation. The laser pulse parameters are  $I_0 = 3 \times 10^{13}$  W/cm $^2$ ,  $\tau = 10$  fs. With vertical dashed lines the 3-6 photon nonsequential transition thresholds measured from the bottom of the  $V_G(R)$  potential energy surface are indicated.

for  $\alpha \in (10^{-1}, 10^{-4})$  was found over which the obtained ionization probability converges and  $\alpha = 0.001$  was chosen to be used throughout all calculations.

## 2. Electron spectra

Calculations for different molecular axis orientations ( $\theta_R \in \{0^\circ, 30^\circ, 60^\circ, 90^\circ\}$ ) have been performed for a fixed laser pulse with the following parameters:  $\lambda = 200$  nm,  $I_0 = 3 \times 10^{13}$  W/cm $^2$ ,  $\tau = 10$  fs. Figure (4) shows the angle integrated ionization probability density as a function of electron ejection energy for  $\theta_R = 0^\circ$  molecular axis orientation. The 3-6 photon transition thresholds measured from the bottom of the  $V_G(R)$  potential energy surface have been plotted with dashed vertical lines. These indicate the location of the non-sequential multiphoton ionization peaks.

In order to better understand the dynamics behind the formation of the multiphoton peaks, Figure (5) shows the angular distribution of the photoelectrons at fixed electron energies sampling the multiphoton peaks from Figure (4). By inspection of the angular distributions, the dominant angular momentum of the ejected electrons in each multiphoton peak can be identified as  $l = 4$ ,  $l = 5$  and  $l = 6$  for the first, second and third multiphoton peak, respectively. Also, knowing that for  $R < 3$  a.u. internuclear separations, the contribution of the  $l = 0$  partial wave to the ground state electronic wave function is greater than 90% leads to the conclusion that the first multiphoton peak is obtained after the absorption of a minimum number of 4 photons. Likewise, it can also be concluded that the second peak

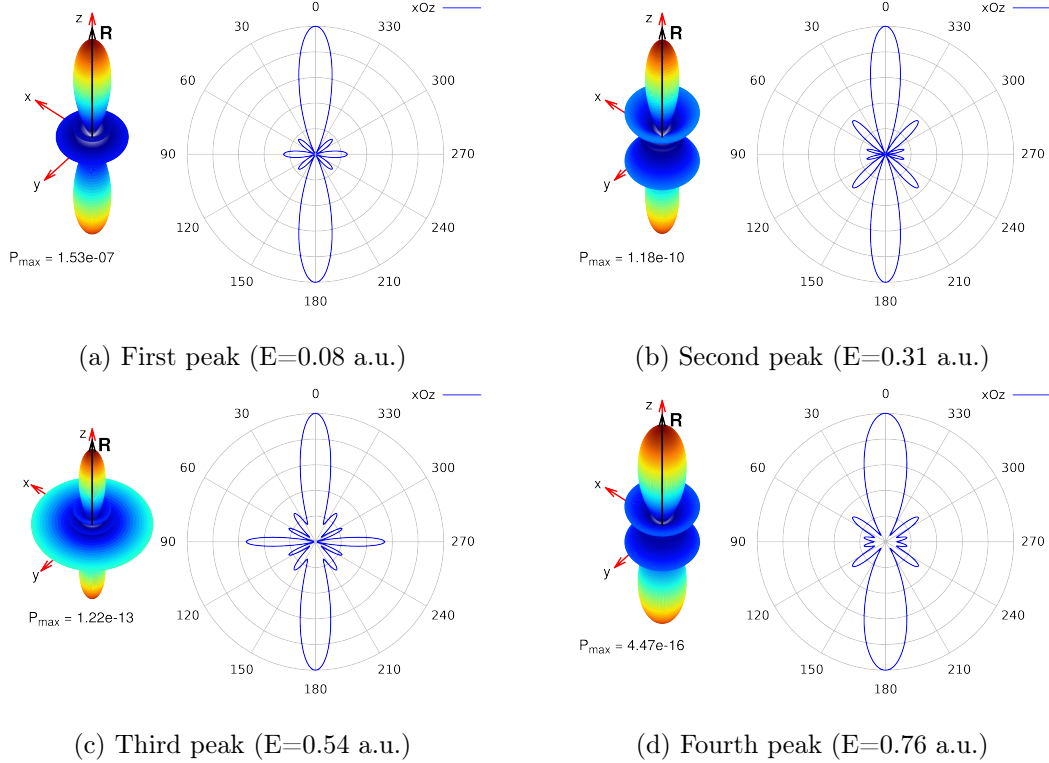


FIG. 5: The ionization probability densities as a function of electron ejection directions for fixed electron energies ( $E$ ) chosen from the multiphoton ionization peaks. The molecular axis ( $R$ ) is fixed along the polarization axis of the laser field ( $Oz$  axis), i.e.  $\theta_R = 0^\circ$ . The spherical plots (left graph in each subfigure) are shown in the reference frame defined in Figure 1. On the polar plots (cuts along the  $xOz$  plane), the ejection angle is measured from the  $Oz$  axis. The maximum of each angular distribution (indicated with  $P_{max}$  on each subfigure) is normalized to 1 for easier comparison.

is a 5-photon process, while the third is a 6-photon one. It can also be observed that there is electron emission perpendicular to the molecular axis (in the  $90^\circ$  and  $270^\circ$  directions) for the first and the third multiphoton peaks indicating that there are continuum electrons only with even angular momentum. An even final state can only be reached from an even ground state by the absorption of an even number of photons. Similarly, the lack of electron emission perpendicular to the molecular axis in the case of the second and fourth multiphoton peaks indicates a final state composed of odd partial waves and the absorption of an odd number of photons. These observations confirm that the order of each multiphoton peak has been correctly identified.

The fact that the 4-photon peak is located on top of the 3-photon non-sequential threshold may be initially misleading but it only indicates that the formation of the multiphoton peak is the result of a sequential process. The most probable scenario is where the molecule

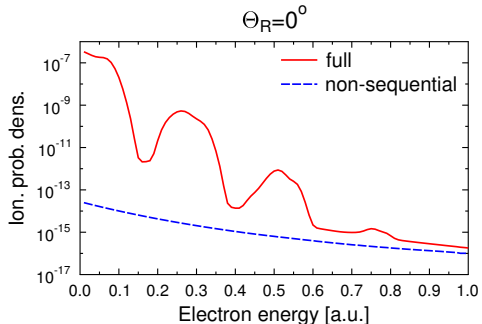


FIG. 6: Same as Figure (4). The results of the full calculations are compared to the results where only the non-sequential ionization pathways are allowed.

is initially excited from the  $V_G$  to the  $V_X$  potential energy surface via a single photon electronic transition. Then the molecule starts to dissociate on the  $V_X$  potential energy surface, while electronic energy is being continuously transferred to the cores. Along this dissociation pathway, the electron may absorb further photons, promoting the system to the  $V_I$  ionization potential energy surface and leading to the observed multiphoton spectrum. The shift of each multiphoton peak compared to its corresponding nonsequential threshold can be attributed to the transfer of electronic energy toward the nuclei.

In order to test the above presented hypothesis, the nonsequential ionization spectrum has been calculated by removing the  $V_X$  potential energy surface from our model, thus removing the sequential ionization pathway. Figure (6) shows the results of these calculations where the electron ejection angle integrated ionization probability is shown as a function of electron energy. These results are compared with those of the full calculation where both the sequential and non-sequential ionization pathways are included. On the figure it can be clearly observed that the contribution of the non-sequential ionization pathway (i.e. direct ionization from the  $V_G$  potential energy surface) to the ionization spectrum is negligible and the dominant ionization pathway is the sequential one.

It can also be observed on Figure (6) that the shape of the full and the non-sequential electron spectrum are significantly different as there are no multiphoton peaks in the non-sequential curve. The source of this discrepancy can be understood from Figure (7), which shows the angular distribution of the photoelectrons at a fixed electron energy ( $E = 0.08$  a.u.). The observable dipole distribution indicates that for these laser field parameters the dominant angular momentum in the non-sequential pathway is  $l = 1$ . This shows that the non-sequential ionization is the result of an one-photon transition and the

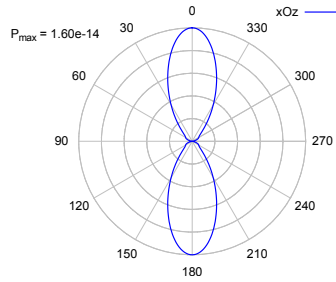


FIG. 7: The angular distribution of the photoelectrons in the xOz plane at the  $E = 0.08$  a.u. electron energy. The maximum of the angular distribution is normalized to 1, and the electron ejection angles are measured from the laser polarization direction (Oz axis), which coincides with the molecular axis ( $\theta_R = 0^\circ$ ).

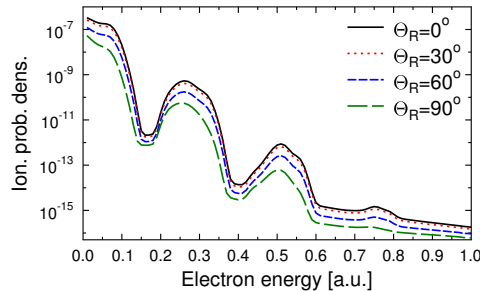


FIG. 8: Angle integrated ionization probability density as a function of electron ejection energy for different  $\theta_R$  molecular axis orientations. The laser pulse parameters are  $I_0 = 3 \times 10^{13}$  W/cm<sup>2</sup>,  $\tau = 10$  fs.

multi-photon transitions contribution is masked by the dominant single-photon contribution. This happens due to the finite duration of the laser pulse used in our calculations, which has a wide spectral bandwidth with slowly decreasing tails.

Attention now turns toward the investigation of the molecular axis orientation dependence of the electron ejection spectra. Figure 8 presents the electron ejection angle integrated ionization probability density as a function of electron energy calculated for different  $\theta_R$  molecular axis orientations. It can be observed that the multiphoton peaks are present in the photoelectron spectrum regardless of the molecular axis orientation. In contrast to this, the total ionization probability density is strongly influenced by the  $\theta_R$  molecular axis orientation. This dependence is shown in Figure 9 where the total ionization probability is presented as a function of the molecular axis orientation ( $\theta_R$ ). The data can be interpreted by considering the transition dipole between a bound and a continuum electronic state which

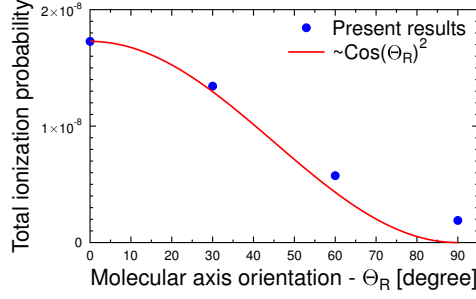


FIG. 9: The total ionization probability as a function of the  $\theta_R$  molecular axis orientations (full circles) are presented along with a normalized  $\cos(\theta_R)^2$  curve. The laser pulse parameters are  $I_0=3 \times 10^{13}$  W/cm<sup>2</sup>,  $\tau = 10$  fs.

can be expressed as

$$\vec{d}(\vec{k}) = \vec{d}_{\parallel}(\vec{k}) + \vec{d}_{\perp}(\vec{k}),$$

where  $\vec{d}_{\parallel}(\vec{k})$  is the component parallel to the molecular axis, while the  $\vec{d}_{\perp}(\vec{k})$  component is perpendicular to the molecular axis and is coplanar with the asymptotic electron momentum  $\vec{k}$ . For small molecular axis orientation angles, the laser coupling between the bound and continuum states is proportional to  $\hat{\epsilon} \vec{d} \simeq \hat{\epsilon} \vec{d}_{\parallel} = d_{\parallel} \cos(\theta_R)$  and thus, the continuum states' population should also be proportional to  $\cos(\theta_R)^2$ . Figure 9 clearly shows that the total ionization probability closely follows the  $\cos(\theta_R)^2$  curve for a large  $\theta_R$  interval. This can be explained by the fact that  $\vec{d}_{\parallel} \gg \vec{d}_{\perp}$ , thus in the  $\vec{\epsilon} \vec{d}$  laser coupling, the  $\vec{\epsilon} \vec{d}_{\perp}$  term has significant contribution only when  $\cos(\theta_R)$  is negligible, i.e. when the molecular axis is nearly perpendicular to the  $\vec{\epsilon}$  laser polarization axis.

The dominance of the  $\hat{\epsilon} \vec{d}_{\parallel}$  term in the laser coupling can also be observed in Figure 10 where the electron ejection angle dependent ionization probability at fixed electron energy ( $E=0.08$  a.u.) is presented for different molecular axis orientations. For a large interval of molecular axis orientations ( $0^\circ < \theta_R < 60^\circ$ ), the shape of the angular distributions is defined by the  $\hat{\epsilon} \vec{d}_{\parallel}$  component of the laser coupling. In this interval, the obtained angular distributions for  $\theta_R \neq 0^\circ$  molecular axis orientations are very similar to the one obtained for  $\theta_R = 0^\circ$ . The angular distribution of the photoelectrons follows the rotation of the molecular axis without any major change in its shape.

Increasing  $\theta_R$  results in the mirror symmetry of the angular distribution relative to the molecular axis in the xOz plane being lost, and the angular distribution tilts in the direction of the laser polarization axis. This effect is caused by  $\hat{\epsilon} \vec{d}_{\perp}$  which in the direction of the laser

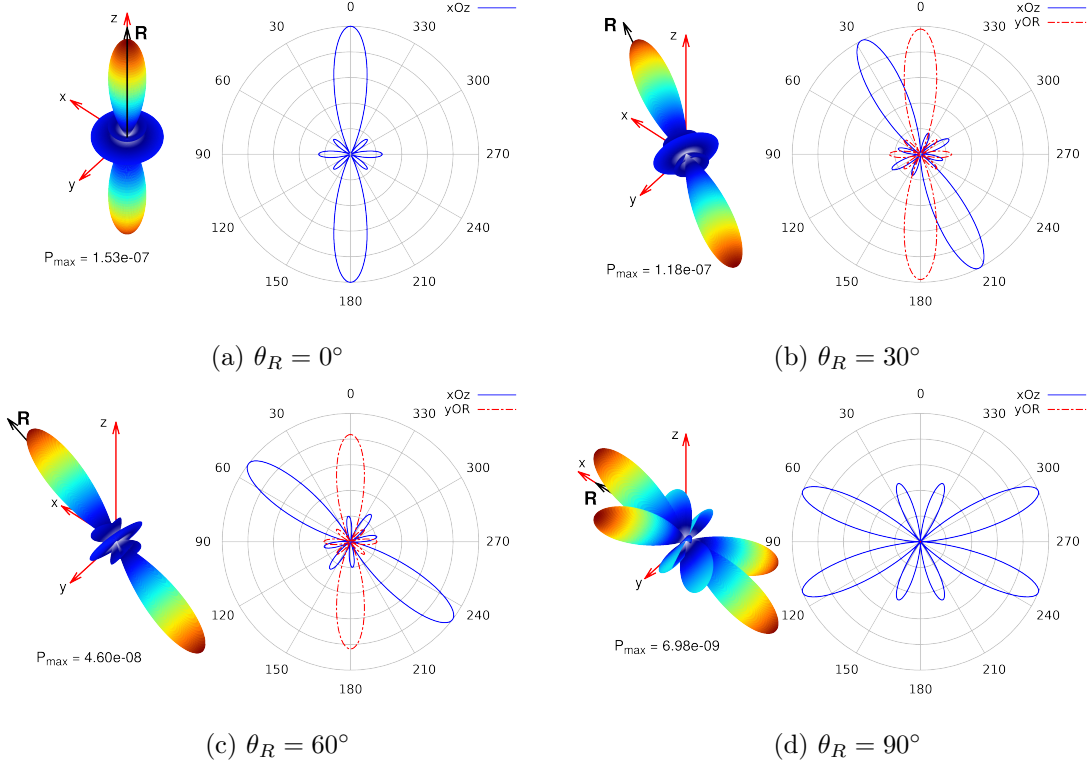


FIG. 10: The ionization probability densities as a function of electron ejection directions are presented for a fixed  $E = 0.08$  a.u. electron energy, and for different molecular axis orientations. The spherical plots (left graph in each subfigure) are shown in the reference frame defined in Figure 1. On the polar plots cuts along the  $xOz$  plane and  $yOR$  planes are presented, where the ejection angle is measured from the  $Oz$  axis ( $xOz$ ) or from  $\vec{R}$  the molecular axis ( $yOR$ ). The maximum of each angular distribution (indicated with  $P_{max}$  on each subfigure) is normalized to 1 for easier comparison.

polarization axis increases whilst in the mirrored direction decreased the laser coupling.

The limiting case of  $\theta_R = 90^\circ$  yields a completely different angular distribution than the other molecular axis orientations. In this case, the laser coupling is solely composed of the  $\hat{\epsilon}\vec{d}_\perp$  term. In contrast to the  $\hat{\epsilon}\vec{d}_\parallel$  term which couples the ground and excited states to continuum states with  $m = 0$  symmetry, the  $\hat{\epsilon}\vec{d}_\perp$  couples the ground and excited states to final states with  $m \neq 0$ . This leads to a continuum composed of partial waves with high  $m$  magnetic quantum number and to the completely different angular distribution observed in Figure 10(d). For the  $\theta_R = 90^\circ$  molecular axis orientation the electron emission in the  $yOR$  plane is forbidden since both the  $\hat{\epsilon}\vec{d}_\perp$  and  $\hat{\epsilon}\vec{d}_\parallel$  terms vanish in this plane.

Figure 10 shows the molecular axis orientation dependence of the angular distribution of photoelectrons only for the first multiphoton peak. Similar behavior can be observed, and the same conclusions can be drawn for the other multiphoton peaks hence we omit their

presentation here.

## B. The HeH<sup>++</sup> system

In order to benchmark our model, calculations have been performed for the ionization of the HeH<sup>++</sup> by XUV laser pulses. and compared the results with the available high precision *ab initio* calculations [52], and with first order perturbation theory calculations. Due to the high photon energy and moderate intensity of the used XUV pulse, the dominant ionization mechanism was single-photon ionization which can be described with high accuracy using first order perturbation theory.

### 1. Technical details

Our model was modified to replicate the available *ab initio* data obtained for fixed molecular axis length and orientation. This fixed-nuclei arrangement can be achieved in the simplest way by adding a masking function to the  $\vec{d}_{ij}(R, \theta_R)$  transition dipole moments:

$$S(R) = \begin{cases} 1 & \text{if } R \in (R_0 - \Delta R, R_0 + \Delta R) \\ 0 & \text{elsewhere} \end{cases}, \quad (19)$$

where  $R_0$  is the fixed molecular axis length. The effect of the  $S(R)$  masking function is that it restricts the transition between the potential energy surfaces to a narrow vicinity of  $R_0$ .

These calculations were performed in a simulation box with  $R_{max} = R_0 + 4.5$  a.u. size and 25 a.u.<sup>-1</sup> gridpoint density. The CAP applied to the ground electronic state was placed at  $R_{max} - 2$  a.u., while on the excited and ionization states a CAP with  $\eta = 0.25$  was placed at  $R_{max} - 1.5$  a.u. For each simulation run, the system was initialized at the ground potential energy surface as a narrow Gaussian wave packet centered around  $R_0$  with a width of 0.05 a.u. The width of the Gaussian wave packets was chosen to prevent it's spreading during the action of the laser pulse and it also perfectly fits in the  $\Delta R = 0.1$  a.u. masking window.

The electronic states and the transition dipole moments between them were calculated by solving the electronic Schrödinger equation directly as outlined in subsection II A. The numerical convergence of the calculated  $\Psi_G(R)$  and  $\Psi_X(R)$  was carefully verified and the

derived potential energy surfaces were in excellent agreement with the *ab initio* data [52].

First order time-dependent perturbation theory [78] calculations were also performed. In this framework the fixed-nuclei transition probability from the ground state to an ionic state with a  $\vec{k}$  continuum electronic momentum can be calculated as

$$P^{1st}(\vec{k}, \vec{R}_0, t) = \left| \left\langle \psi_c(\vec{k}, \vec{r}) | \vec{\epsilon} \vec{r} | \psi_G(\vec{R}_0, \vec{r}) \right\rangle \int_0^t dt' F(t') e^{i[\frac{k^2}{2} - E_G(R_0)]t'} \right|^2, \quad (20)$$

where all components (ground and continuum electronic wave functions, shape of the electric field) are already known.

## 2. Energy integrated angular distribution of photoelectrons

We have calculated the ionization probability density of the  $\text{HeH}^{++}$  molecular ion interacting with an XUV ultrashort laser pulse. In accordance to [52] the photon energy was chosen to be 200 eV, the duration of the pulse was fixed at 25 optical cycles, while the intensity at  $I_0 = 10^{13}$  W/cm<sup>2</sup>. Figure 11 shows a good agreement of our results for different molecular axis lengths ( $R$ ) with the reference data of Guan et. al [52] at the level of electron momentum integrated angular distribution of photoelectrons. For an easier comparison all presented data are normalized to their maximum. In contrast to the  $\text{D}_2^+$  situation where the behaviour of the photoelectron angular distributions as a function of molecular axis orientations has been extensively investigated, this study is constrained to the case of molecular axis orientation parallel to the laser polarization axis. Regardless of the molecular axis length the electron emission in all models is predominantly occurring in the direction of the H core ( $\sim 180$  degrees). The agreement between our present model and the first order perturbation calculations with fixed nuclei is excellent. This is not surprising since both use the same initial and final electronic states. This agreement suggests, that the inclusion of the masking function  $S(R)$  (19) in our model is a suitable approach to reproduce fixed-nuclei calculations. There are also discrepancies between the reference [52] and the present *ab initio* results. Our model underestimates the electron emission in the direction of the He core and presents a different shape of the angular distribution perpendicular to the molecular axis (between 60 and 120 degrees). These discrepancies are assumed to be caused by the different description of the continuum electrons. In our model, simple one-center Coulomb

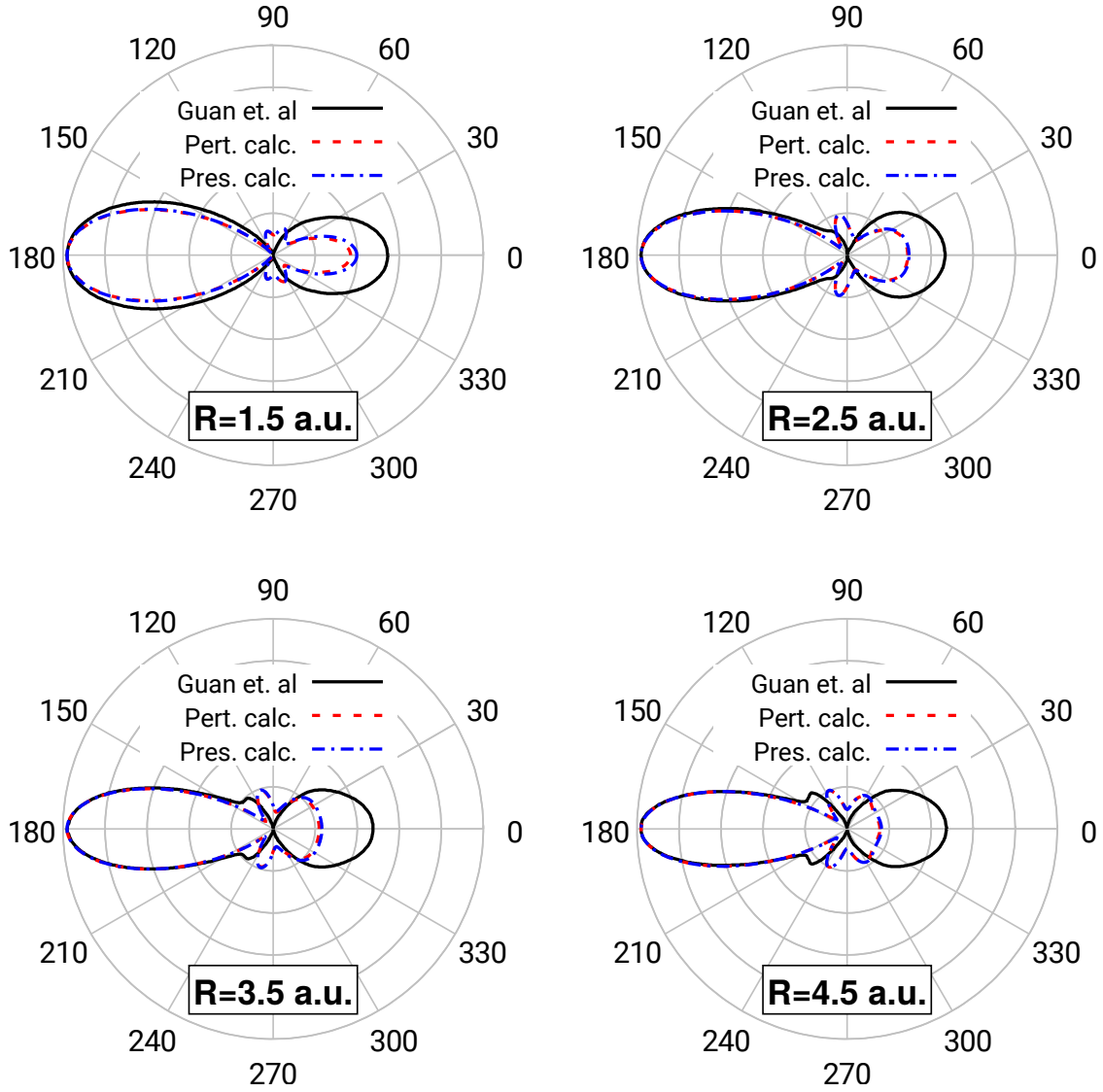


FIG. 11: The electron momentum integrated angular distribution of photoelectrons emitted by  $\text{HeH}^{++}$  for different fixed molecular axis lengths. The molecular axis orientation is also fixed in the direction of laser polarization vector. The results of the *ab initio* and perturbative calculations are compared with the results of Guan et. al [52]. The length of the laser pulse was fixed at 25 optical cycles, the photon energy was 200 eV, while the intensity was set to  $I_0 = 10^{13} \text{W}/\text{cm}^2$ .

wave functions (see Eq. 14) centered at the charge center of the molecule are used while Guan et. al [52] uses the exact two-center Coulomb wave functions. This indicates that our model would be improved by switching to the two-center Coulomb wave functions for the description of the continuum electrons.

## IV. CONCLUSIONS AND OUTLOOK

In the present paper we have developed and tested a simple model for the *ab initio* description of the combined electronic and nuclear motion of diatomics with a single active electron. In the framework of this model, we have followed the nuclear motion on electronic potential energy surfaces which have an important role in the dynamics. We have extended an existing approach [10–17] which considered only bound electronic states in the dynamics by including the potential energy surfaces corresponding to ionized states. This way, beside the dissociation we were also able to study the ionization. Continuum-continuum transitions and the ground state depletion effects are neglected by the present model as the calculations for different ionization states are performed independently.

Within the framework of this model, we have performed test calculations for the multiphoton ionization of the  $D_2^+$  molecule, and we have analyzed in details the resulting ionization spectra. The energy and angular dependence of the obtained data could be explained using simple arguments.

The model was then benchmarked using the ionization of  $HeH^{++}$  in the single-photon regime and our results were compared to the reference data of Guan et. al [52]. There was a good agreement between the two data sets, however small discrepancies were also identified pointing out possible ways of improving our approach.

The reliability of our model in the single and multiphoton ionization regimes shown throughout these test calculations gives us a solid base for the further improvement of the model. In the next step, the kinetic energy release (KER) spectrum for both the dissociation and ionization channels will be calculated for fixed molecular axis orientations. The model will then be further improved by including the rotational degree of freedom as well. At that stage of development, we will be able to study how the LICI is influencing both the electronic and KER spectrum.

## ACKNOWLEDGMENT

The authors acknowledge the financial support by a grant of the Romanian National Authority for Scientific Research project number PN-II-ID-PCE-2011-3-0192, by the European COST Action CM1204 XLIC and by the TAMOP-4.2.2.B-15/1/KONV-2015-0001. Á.V. and

S. B. also acknowledge the OTKA (NN103251 and K103917) projects. Financial support by the Hungarian Academy of Sciences is gratefully acknowledged. The authors thank Lorenz Cederbaum for many valuable discussions.

---

- [1] M. Born and J. R. Oppenheimer, *Ann. Phys.* **84**, 457 (1927).
- [2] H. Köppel, W. Domcke, and L. S. Cederbaum, *Adv. Chem. Phys.* **57**, 59 (1984).
- [3] M. Baer, *Physics Reports* **358**, 75 (2002).
- [4] G. A. Worth and L. S. Cederbaum, *ANNUAL REVIEW OF PHYSICAL CHEMISTRY* **55**, 127 (2004).
- [5] W. Domcke, D. R. Yarkony, and H. Köppel, *Conical Intersections: Electronic Structure, Dynamics & Spectroscopy* (World Scientific Publishing Co., 2004).
- [6] M. Baer, *Beyond Born-Oppenheimer: Electronic Nonadiabatic Coupling Terms and Conical Intersections* (Wiley, 2006).
- [7] S. Matsika, *Rev. Comput. Chem* **23**, 83 (2007).
- [8] N. Moiseyev, M. Šindelka, and L. S. Cederbaum, *J. Phys. B.* **41**, 221001 (2008).
- [9] M. Šindelka, N. Moiseyev, and L. S. Cederbaum, *J. Phys. B.* **44**, 045603 (2011).
- [10] G. J. Halász, Á. Vibók, M. Šindelka, N. Moiseyev, and L. S. Cederbaum, *Journal of Physics B: Atomic, Molecular and Optical Physics* **44**, 175102 (2011).
- [11] G. J. Halász, M. Šindelka, N. Moiseyev, L. S. Cederbaum, and Á. Vibók, *The Journal of Physical Chemistry A* **116**, 2636 (2012).
- [12] G. J. Halász, Á. Vibók, M. Šindelka, L. S. Cederbaum, and N. Moiseyev, *Chemical Physics* **399**, 146 (2012), new trends in atomic and molecular clusters.
- [13] G. J. Halász, Á. Vibók, N. Moiseyev, and L. S. Cederbaum, *Journal of Physics B: Atomic, Molecular and Optical Physics* **45**, 135101 (2012).
- [14] G. J. Halász, Á. Vibók, H.-D. Meyer, and L. S. Cederbaum, *The Journal of Physical Chemistry A* **117**, 8528 (2013).
- [15] G. J. Halász, Á. Vibók, N. Moiseyev, and L. S. Cederbaum, *Phys. Rev. A* **88**, 043413 (2013).
- [16] G. J. Halász, A. Csehi, Á. Vibók, and L. S. Cederbaum, *The Journal of Physical Chemistry A* **118**, 11908 (2014).

- [17] G. J. Halász, Á. Vibók, and L. S. Cederbaum, *The Journal of Physical Chemistry Letters* **6**, 348 (2015).
- [18] A. Zavriyev, P. H. Bucksbaum, H. G. Muller, and D. W. Schumacher, *Phys. Rev. A* **42**, 5500 (1990).
- [19] A. D. Bandrauk and M. L. Sink, *Chemical Physics Letters* **57**, 569 (1978).
- [20] A. D. Bandrauk and M. L. Sink, *J. Chem. Phys.* **74**, 1110 (1981).
- [21] E. E. Aubanel, J.-M. Gauthier, and A. D. Bandrauk, *Phys. Rev. A* **48**, 2145 (1993).
- [22] E. Charron, A. Giusti-Suzor, and F. H. Mies, *Phys. Rev. A* **49**, R641 (1994).
- [23] S. Chelkowski, T. Zuo, O. Atabek, and A. D. Bandrauk, *Phys. Rev. A* **52**, 2977 (1995).
- [24] A. Giusti-Suzor, F. H. Mies, L. F. DiMauro, E. Charron, and B. Yang, *Journal of Physics B: Atomic, Molecular and Optical Physics* **28**, 309 (1995).
- [25] R. Numico, A. Keller, and O. Atabek, *Phys. Rev. A* **52**, 1298 (1995).
- [26] K. Sändig, H. Figger, and T. W. Hänsch, *Phys. Rev. Lett.* **85**, 4876 (2000).
- [27] V. N. Serov, A. Keller, O. Atabek, and N. Billy, *Phys. Rev. A* **68**, 053401 (2003).
- [28] J. H. Posthumus, *Reports on Progress in Physics* **67**, 623 (2004).
- [29] V. Serov, A. Keller, O. Atabek, H. Figger, and D. Pavicic, *Phys. Rev. A* **72**, 033413 (2005).
- [30] M. Uhlmann, T. Kunert, and R. Schmidt, *Phys. Rev. A* **72**, 045402 (2005).
- [31] P. Q. Wang, A. M. Saylor, K. D. Carnes, J. F. Xia, M. A. Smith, B. D. Esry, and I. Ben-Itzhak, *Phys. Rev. A* **74**, 043411 (2006).
- [32] F. Anis and B. D. Esry, *Phys. Rev. A* **77**, 033416 (2008).
- [33] F. Anis, T. Cackowski, and B. D. Esry, *Journal of Physics B: Atomic, Molecular and Optical Physics* **42**, 091001 (2009).
- [34] J. J. Hua and B. D. Esry, *Phys. Rev. A* **80**, 013413 (2009).
- [35] A. K. Paul, S. Adhikari, D. Mukhopadhyay, G. J. Halász, Á. Vibók, R. Baer, and M. Baer, *The Journal of Physical Chemistry A* **113**, 7331 (2009).
- [36] A. K. Paul, S. Adhikari, M. Baer, and R. Baer, *Phys. Rev. A* **81**, 013412 (2010).
- [37] U. Thumm, T. Niederhausen, and B. Feuerstein, *Phys. Rev. A* **77**, 063401 (2008).
- [38] M. Fischer, F. Grossmann, R. Schmidt, J. Handt, S. M. Krause, and J.-M. Rost, *New Journal of Physics* **13**, 053019 (2011).
- [39] M. Fischer, U. Lorenz, B. Schmidt, and R. Schmidt, *Phys. Rev. A* **84**, 033422 (2011).

- [40] J. McKenna, F. Anis, A. M. Sayler, B. Gaire, N. G. Johnson, E. Parke, K. D. Carnes, B. D. Esry, and I. Ben-Itzhak, *Phys. Rev. A* **85**, 023405 (2012).
- [41] H.-X. He, R.-F. Lu, P.-Y. Zhang, K.-L. Han, and G.-Z. He, *The Journal of Chemical Physics* **136**, 024311 (2012).
- [42] Y. Furukawa, Y. Nabekawa, T. Okino, A. A. Eilanlou, E. J. Takahashi, P. Lan, K. L. Ishikawa, T. Sato, K. Yamanouchi, and K. Midorikawa, *Opt. Lett.* **37**, 2922 (2012).
- [43] H. He, R. Lu, P. Zhang, Y. Guo, K. Han, and G. He, *Phys. Rev. A* **84**, 033418 (2011).
- [44] M. Magrakvelidze, F. He, T. Niederhausen, I. V. Litvinyuk, and U. Thumm, *Phys. Rev. A* **79**, 033410 (2009).
- [45] F. He and U. Thumm, *Phys. Rev. A* **81**, 053413 (2010).
- [46] I. Ben-Itzhak, P. Q. Wang, J. F. Xia, A. M. Sayler, M. A. Smith, K. D. Carnes, and B. D. Esry, *Phys. Rev. Lett.* **95**, 073002 (2005).
- [47] M. Fischer, J. Handt, J.-M. Rost, F. Grossmann, and R. Schmidt, *Phys. Rev. A* **86**, 053821 (2012).
- [48] C. Lefebvre, T. T. Nguyen-Dang, F. Dion, M. J. J. Vrakking, V. N. Serov, and O. Atabek, *Phys. Rev. A* **88**, 053416 (2013).
- [49] A. Apalategui, A. Saenz, and P. Lambropoulos, *Journal of Physics B: Atomic, Molecular and Optical Physics* **33**, 2791 (2000).
- [50] S. Chelkowski, A. D. Bandrauk, A. Staudte, and P. B. Corkum, *Phys. Rev. A* **76**, 013405 (2007).
- [51] D. I. R. Boll and O. A. Fojón, *Journal of Physics: Conference Series* **583**, 012033 (2015).
- [52] X. Guan, E. B. Secor, R. C. DuToit, and K. Bartschat, *Phys. Rev. A* **86**, 053425 (2012).
- [53] K.-J. Yuan, S. Chelkowski, and A. D. Bandrauk, *The Journal of Chemical Physics* **142**, 144304 (2015).
- [54] J. Handt, S. M. Krause, J.-M. Rost, M. Fischer, F. Grossmann, and R. Schmidt, *ArXiv* , 1103.1565v2 (2011).
- [55] D. Pavicic, A. Kiess, T. Hänsch, and H. Figger, *The European Physical Journal D - Atomic, Molecular, Optical and Plasma Physics* **26**, 39 (2003).
- [56] D. Pavičić, A. Kiess, T. W. Hänsch, and H. Figger, *Phys. Rev. Lett.* **94**, 163002 (2005).
- [57] S. Selstø, A. Palacios, J. Fernández, and F. Martín, *Phys. Rev. A* **75**, 033419 (2007).

- [58] J. Fernández, F. L. Yip, T. N. Rescigno, C. W. McCurdy, and F. Martín, *Phys. Rev. A* **79**, 043409 (2009).
- [59] F. Kelkensberg, C. Lefebvre, W. Siu, O. Ghafur, T. T. Nguyen-Dang, O. Atabek, A. Keller, V. Serov, P. Johnsson, M. Swoboda, T. Remetter, A. L’Huillier, S. Zherebtsov, G. Sansone, E. Benedetti, F. Ferrari, M. Nisoli, F. Lépine, M. F. Kling, and M. J. J. Vrakking, *Phys. Rev. Lett.* **103**, 123005 (2009).
- [60] A. Picón, A. Bahabad, H. C. Kapteyn, M. M. Murnane, and A. Becker, *Phys. Rev. A* **83**, 013414 (2011).
- [61] A. R. Bainbridge, J. Harrington, A. Kirrander, C. Cacho, E. Springate, W. A. Bryan, and R. S. Minns, *New Journal of Physics* **17**, 103013 (2015).
- [62] Nabekawa Yasuo, Furukawa Yusuke, Okino Tomoya, Amani Eilanlou A., Takahashi Eiji J., Yamanouchi Kaoru, and Midorikawa Katsumi, *Nat Commun* **6:8197** (2015), 10.1038/ncomms9197, supplementary information available for this article at [http://www.nature.com/ncomms/2015/150901/ncomms9197/supinfo/ncomms9197\\_S1.html](http://www.nature.com/ncomms/2015/150901/ncomms9197/supinfo/ncomms9197_S1.html).
- [63] E. Khosravi, A. Abedi, and N. T. Maitra, *Phys. Rev. Lett.* **115**, 263002 (2015).
- [64] H. Xu, F. He, D. Kielpinski, R. T. Sang, and I. V. Litvinyuk, *Scientific Reports* **5**, 13627 (2015).
- [65] V. Wanie, H. Ibrahim, S. Beaulieu, N. Thiré, B. E. Schmidt, Y. Deng, A. S. Alnaser, I. V. Litvinyuk, X.-M. Tong, and F. Légaré, *Journal of Physics B: Atomic, Molecular and Optical Physics* **49**, 025601 (2016).
- [66] H.-D. Meyer, U. Manthe, and L. Cederbaum, *Chemical Physics Letters* **165**, 73 (1990).
- [67] U. Manthe, H.-D. Meyer, and L. S. Cederbaum, *J. Chem. Phys.* **97**, 3199 (1992).
- [68] M. Beck, A. Jäckle, G. Worth, and H.-D. Meyer, *Physics Reports* **324**, 1 (2000).
- [69] G. A. Worth, *The MCTDH package: vesion 8.2* (University of Heidelberg, 2000).
- [70] H.-D. Meyer, *The MCTDH package: vesion 8.3 and 8.4* (University of Heidelberg, 2002 and 2007).
- [71] H.-D. Meyer, F. Gatti, and G. A. Worth, *Multidimensional Quantum Dynamics: MCTDH Theory and Applications* (Wiley-VCH, 2009).
- [72] T. N. Rescigno and C. W. McCurdy, *Phys. Rev. A* **62**, 032706 (2000).
- [73] V. Hernandez, J. E. Roman, and V. Vidal, *ACM Transactions on Mathematical Software (TOMS)* **31**, 351 (2005).

- [74] G.-Z. Kiss, S. Borbély, and L. Nagy, AIP Conference Proceedings **1694**, 020017 (2015).
- [75] A. Messiah, *Quantum Mechanics*, Dover Books on Physics (Dover Publications Inc., 2014).
- [76] F. V. Bunkin and I. I. Tugov, Phys. Rev. A **8**, 601 (1973).
- [77] S. I. Chu, C. Laughlin, and K. K. Datta, Chem. Phys. Lett. **98**, 476 (1983).
- [78] B. H. Bransden and C. J. Joachain, *Physics of atoms and molecules* (Longman Scientific & Technical, 1983).